Geophysical Research Letters

RESEARCH LETTER
10.1029/2025GL114704

Key Points:

- X-ray computed tomography and Raman spectroscopy together can accurately measure the composition of polymineralic inclusions in diamond
- The Ti content of former CaSi-perovskite inclusions in sublithospheric diamonds resembles experimental studies on subduction zone basalt
- Ti content of former CaSi-perovskite inclusions appears to be a function of the formation depth of the diamond

Supporting Information:

Supporting Information may be found in the online version of this article.

Correspondence to:
B. D. Rayner,
ucfbwdr@ucl.ac.uk

Citation:
Rayner, B. D., Kohn, S. C., Garwood, R. J., Burnham, A. D., Bulanova, G. P., Smith, C. B., & Thomson, A. R. (2025). Correlative tomography for polymineralic inclusion composition in sublithospheric diamonds. *Geophysical Research Letters*, *52*, e2025GL114704. https://doi.org/10.1029/2025GL114704

Received 6 JAN 2025
Accepted 27 MAY 2025

Author Contributions:
Data curation: B. D. Rayner
Formal analysis: B. D. Rayner, S. C. Kohn, R. J. Garwood
Funding acquisition: S. C. Kohn
Investigation: B. D. Rayner, S. C. Kohn, R. J. Garwood, A. D. Burnham, G. P. Bulanova, C. B. Smith, A. R. Thomson
Methodology: B. D. Rayner, S. C. Kohn, R. J. Garwood, A. D. Burnham, A. R. Thomson
Project administration: S. C. Kohn
Supervision: S. C. Kohn, G. P. Bulanova, C. B. Smith, A. R. Thomson
Writing – original draft: B. D. Rayner

Correlative Tomography for Polymineralic Inclusion Composition in Sublithospheric Diamonds

B. D. Rayner[1,2], S. C. Kohn[1], R. J. Garwood[3,4], A. D. Burnham[5], G. P. Bulanova[1], C. B. Smith[1], and A. R. Thomson[2,4]

[1]School of Earth Sciences, University of Bristol, Bristol, UK, [2]Department of Earth Sciences, University College London, London, UK, [3]Department of Earth and Environmental Sciences, University of Manchester, Manchester, UK, [4]The Natural History Museum, London, UK, [5]Research School of Earth Sciences, Australian National University, Canberra, ACT, Australia

Abstract Sublithospheric diamonds and their inclusions are the deepest known samples from the Earth's mantle. Typically, the inclusions are trapped as minerals which are only stable in the deep mantle, retrogressing into multiple phases during their uplift. Determining the bulk inclusion composition is difficult but crucially important. Here we use micron-scale synchrotron X-ray computed tomography alongside μ-Raman mapping to reconstruct primary inclusion compositions of seven former Ti-rich CaSi-perovskite inclusions, which had retrogressed to assemblages of breyite and perovskite. The inclusions display Ti#s (molar Ti/[Ti + Si]), ranging from 0.03 to 0.60. In diamonds with previously reported coexisting inclusions, former bridgmanite coexists with lower Ti# CaSi-perovskite and garnet inclusions with higher Ti# CaSi-perovskite. This observation is consistent with published petrological experiments on mafic compositions suggesting that CaSi-perovskite undergoes a decrease in Ti# after the post-garnet transition. Thus variations in Ti content of CaSi-perovskite inclusions are interpreted as differences in formation pressures.

Plain Language Summary Material sourced directly from deep within the Earth's mantle is extremely rare and sublithospheric diamonds are therefore uniquely valuable. As these diamonds grow they trap mineral inclusions from their environment and upon ascent to the surface these inclusions depressurize and decompose into multiple minerals with different compositions. This makes it difficult to measure the compositions of the originally captured minerals, and thus how and where they formed. Here we apply X-ray computed tomography to image these inclusions in three dimensions to reconstruct their original compositions. We find that these compositions match those expected to occur in cold crustal rock as it sinks through the mantle.

1. Introduction

Diamonds form at high pressure within the Earth and as they grow, they capture mineral inclusions from their formation environment, the compositions of which can indicate the conditions of diamond formation. Diamonds derived from below the lithosphere are called sublithospheric diamonds, and can contain inclusions of minerals that are not stable at shallower conditions. These inclusions often retrogress into one or more phases upon ascent (Harte & Hudson, 2013; Stachel et al., 2000; Walter et al., 2011), producing polymineralic inclusions. Inclusions containing both breyite ($CaSiO_3$) and perovskite ($CaTiO_3$) are among the most common inclusion types within meta-basaltic sublithospheric diamonds (Walter et al., 2022). Breyite is a high pressure mineral found exclusively in sublithospheric diamonds inclusions (Brenker et al., 2021), and is often interpreted as retrograde CaSi-perovskite, although in single phase inclusions without perovskite this remains controversial (Woodland et al., 2020). Here, breyite-perovskite inclusions are interpreted as retrogressed high-Ti CaSi-perovskite ($Ca[Si,Ti]O_3$); no other known precursor calcium silicate mineral with ABO_3 stoichiometry could be sufficiently Ti-rich and it is extremely unlikely that any other material, such as multiple minerals or a melt, could reproduce this precise stoichiometry as frequently as observed. Walter et al. (2022) describe two populations of former CaSi-perovskite, referred to as "high-Ti" (>2 wt% TiO_2) and "low-Ti" (<0.7 wt% TiO_2). Breyite-perovskite inclusions in the literature are almost all "high-Ti," indicating derivation from subducted mafic crust (Walter et al., 2022), but it is unclear what causes the significant variation in Ti content within this group.

Determining the bulk compositions of polymineralic inclusions accurately is difficult. Methods used previously are all subject to considerable limitations and are as follows:

Writing – review & editing:
B. D. Rayner, S. C. Kohn, R. J. Garwood, A. D. Burnham, G. P. Bulanova, C. B. Smith, A. R. Thomson

(i) Crushing the host diamond and recovering inclusions from the debris (e.g., Harte & Cayzer, 2007; Hayman et al., 2005; Stachel et al., 2000). The outside surfaces, or planes polished into the picked inclusions, are then examined by X-ray spectroscopy using a scanning electron microscope. This method risks dissociating or even losing parts of the inclusion, which inhibits its ability to quantitatively assess the abundance of phases.

(ii) Polishing diamonds to expose inclusions at the surface and using electron microbeam techniques to measure composition. Two variations include:

  a. Individual phases within the inclusion are analysed with a focussed beam and bulk compositions are calculated using each phase's relative area on the exposed surface (Bulanova et al., 2010; Harte & Cayzer, 2007; Thomson et al., 2014). This assumes that the exposed area of each phase is representative of its volumetric abundance within the whole inclusion and that all phases within the inclusion are exposed or have not been polished away. Figure 1 illustrates how unlikely this is to be the case.

  b. The inclusion's exposed area is analysed using a broad, defocussed, electron beam (Thomson et al., 2014; Walter et al., 2011). For small inclusions, the analytical volume is a significant fraction of the inclusion, and recovered analyses may approach the true bulk chemistry. Nonetheless, this method also assumes that no phases were destroyed during polishing or are too deep within the inclusion to measure. Moreover, the matrix corrections used in electron probe microanalysis assume a homogeneous volume of infinite size, which is not true of a polymineralic inclusion surrounded by a low-Z matrix such as diamond that minimally attenuates X-rays (Bence & Albee, 1968).

These methods all involve the partial destruction of diamonds and inclusions. Non-destructive alternatives are attractive as they allow the maximum amount of data to be derived from these exceptionally rare samples in the future. X-ray computed microtomography (µCT), combined with knowledge of the inclusion's chemistry gained through techniques applicable in situ such as Raman spectroscopy, X-ray diffraction or X-ray Fluorescence, could be used to determine a polymineralic inclusion's bulk composition accurately and non-destructively by imaging its entire volume. µCT has previously been used to study diamond inclusions in situ (Agrosi et al., 2019; Jacob et al., 2011; Ketcham & Koeberl, 2013; Nestola et al., 2012), but never for this purpose. Here we demonstrate a technique for determination of the bulk composition of breyite-perovskite inclusions.

2. Materials and Methods

2.1. Sublithospheric Diamonds From Juina Area, Brazil

The seven diamonds studied here originate from the Juina-5 and Collier-4 kimberlite pipes in Juina, Brazil (specimen numbers are provided in Table 1) and are of sublithospheric, subduction-related origin. Previous work on these diamonds includes work by Walter et al. (2008, 2011), Bulanova et al. (2010), Thomson et al. (2014), Burnham et al. (2015), Thomson, Kohn, et al. (2016), and Timmerman et al. (2023). The diamonds each contain at least one breyite-perovskite inclusion.

2.2. Bulk Composition Reconstructions

Determining the bulk compositions of polymineralic inclusions requires knowledge of the composition, volume and density (in order to convert volumes to molar ratio) of each of the constituent phases in the inclusions. For the case of breyite-perovskite inclusions, these can all be determined using µCT combined with Raman spectroscopy, but additional techniques may be required when investigating different inclusion mineralogies.

2.2.1. Composition Estimates From Raman Spectroscopy

Raman spectra and micron-resolution maps were collected with a Thermo DXRxi spectrometer at the University of Bristol. Data on the conditions of each analysis can be found in Supporting Information S1. The analysis of sample Ju5-52 was performed on a Thermo DXR microscope. Phase identification was performed with reference to library examples.

Breyite has no significant solid solutions (Brenker et al., 2021), so it is assumed that all breyite regions in inclusions consist of pure $CaSiO_3$. In contrast, the equilibrium Ti-Si ratio of perovskite coexisting with breyite in the $CaSiO_3$-$CaTiO_3$ system varies with pressure (Kubo et al., 1997). As majoritic garnet inclusions from these diamonds demonstrate high equilibration pressures (Thomson et al., 2021) it is important to constrain the perovskite Ti# (molar Ti/[Ti + Si]) when calculating bulk breyite-perovskite inclusion compositions.

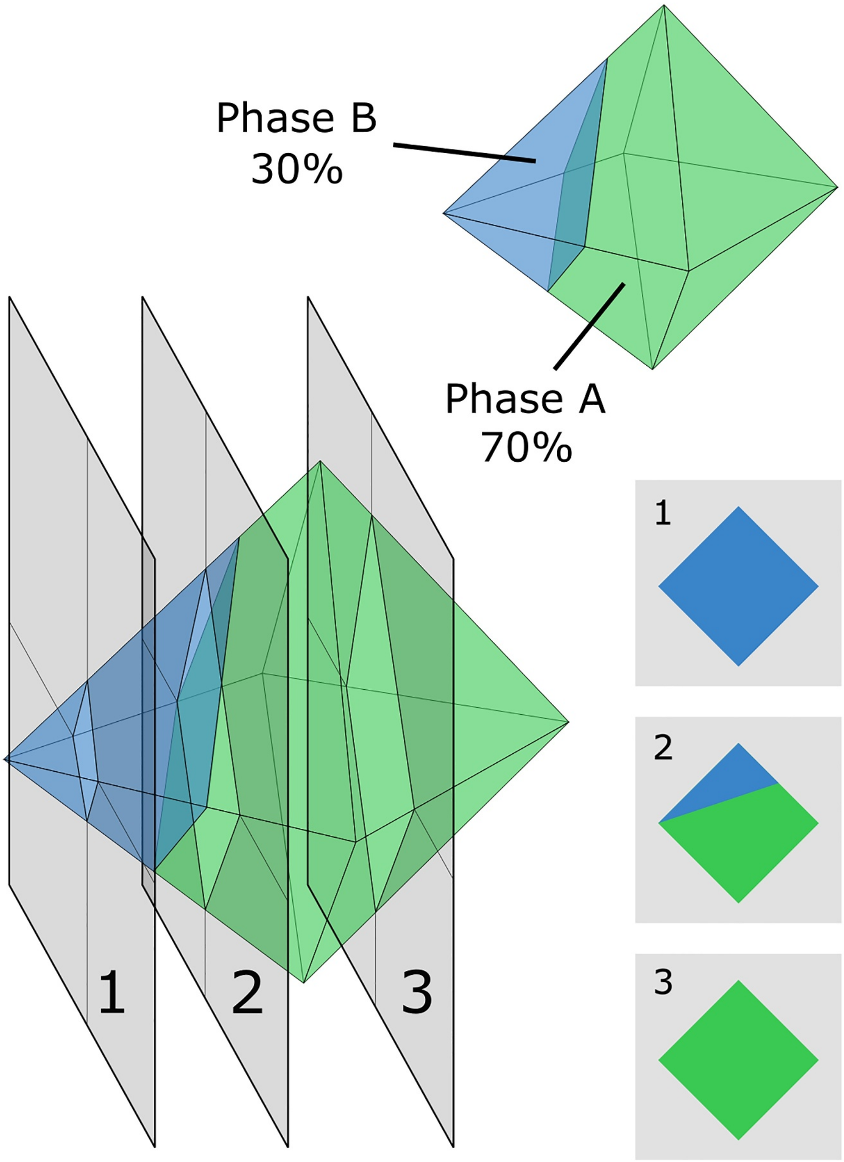

Figure 1. Schematic of a two-phase inclusion showing how different exposed surfaces could give unrepresentative estimates of phase proportions. The three polished planes shown could contain all B, all A or anything intermediate.

The Si-content of each perovskite can be established using the peak positions of the collected Raman spectra. CaSi-perovskite has a smaller unit cell volume than pure $CaTiO_3$ perovskite (Thomson et al., 2025) and Raman peak positions vary with chemistry; the ~780 cm^{-1} peak (in $CaTiO_3$) increases in frequency with increasing $CaSiO_3$ component. We utilize a Raman frequency composition relationship produced by Thomson et al. (2025): mol% $CaSiO_3 = 0.46 * (\nu - 772.8)$ where ν is the Raman frequency of the 780 cm^{-1} peak. However, increasing pressure also produces an upward shift of 5.78 cm^{-1}/GPa in this Raman peak (Guennou et al., 2010), so a correction is required to avoid overestimating the Si-content in perovskite inclusions with remanent pressure (which can be up to 5.4 GPa (Genzel et al., 2023)). Combining the two relationships produces a simple pressure correction on the Raman frequency-composition relationship of 2.659 mol% $CaSiO_3$/GPa, that is, for every GPa of remanent pressure, 2.659 mol% is subtracted from the perovskite component's $CaSiO_3$ content.

Internal pressures were evaluated using the breyite barometer of Anzolini et al. (2018)—which uses the positive linear relationship between pressure and the frequency of the 977 cm^{-1} peak.

Table 1
Data Summary

Diamond		Ju5-52		Ju5-13		Col-N-4	Ju5-104	Ju5-119	Col-N-18		Ju5-82
Lens objective in acquisition:		10×	4×	10×	4×	4×	4×	4×	10×	4×	4×
Vol % of perovskite from μCT:		2.9(4)	2.9(3)	3.9(4)	4.2(2)	7.3(8)	10.1(8)	11.3(34)	21.0(12)	25.2(10)	53.8(41)
Internal pressure (GPa):		1.0		1.7		2.3	2.1	0.0	1.2		1.0
Perovskite mol% $CaSiO_3$ from Raman:		n/a		3.0		5.3	7.1	9.8	5.2		8.9
Density (g/cm^3)	Breyite	3.09		3.16		3.18	3.17	3.09	3.14		3.13
	Perovskite, $CaTiO_3$	4.04		4.07		4.09	4.08	4.04	4.06		4.06
	Perovskite, high $CaSiO_3$	n/a		4.08		4.09	4.09	4.05	4.07		4.07
Calculated bulk Ti#		0.033(5)	0.032(4)	0.043(5)	0.045(3)	0.078(1)	0.11(12)	0.12(41)	0.22(18)	0.27(16)	0.54(65)

Note. Volume ratio derived from μCT and calculated bulk Ti# are given as the mean of the maximum and minimum constraints, alongside half the range. * Perovskite Raman spectrum from Ju5-52 was not acquired, so maximum constraint on Ti# was calculated using $CaTiO_3$ perovskite component.

This technique assumes that these perovskites are an ideal $CaTiO_3$-$CaSiO_3$ mixture with no otherwise negligible impurities present, reasonable to expect in natural perovskites. This may affect the Raman spectra and cause an over-estimation of perovskite Si contents. Therefore they are treated as maximum constraints only.

2.2.2. Volume Reconstructions From μCT

Coherent, pink-beam synchrotron μCT imaging was used to recover the volume fraction of inclusion phases. Measurements were conducted at the I13 beamline of Diamond Light Source. 1,800 projections were collected over a 180° rotation on a pco.edge 5.5 sCMOS Camera using 4× (0.05 s exposures; 0.81 μm voxels) and/or 10× (0.3 s exposures; 0.33 μm voxels) objective lenses. All samples were initially studied using the 4× objective, whilst time allowed only some to be restudied at higher resolution.

Computed tomograms were reconstructed using DAWN (Basham et al., 2015), and subsequently analysed using the Drishti 2.7 (Hu et al., 2020), SPIERS 3.0.0 (Sutton et al., 2012) and ImageJ 1.54d packages. 32-bit floating point tiffs were loaded in Drishti import, the histogram was windowed to cover the lightest and darkest voxels, and the data sets were exported as 8-bit PNG stacks. For noisier data sets—all 10× scans and two of the 4× scans from diamonds Ju5-52 and Col-N-18—2D mean filter smoothing was applied slice-by-slice using ImageJ. Data sets were imported into SPIERSedit for volume measurements. This was achieved using the segments tool, which allows a gray level range (between "threshold" values) to be assigned to a particular phase. Tomogram greyscale corresponds to the average X-ray attenuation of the material at each point in the reconstructed volume. In this instance the darkest, hence the least X-ray attenuating, region surrounding each inclusion is diamond. The brightest phase observed is perovskite: the high Ti content provides a greater mean atomic density, and so higher attenuation, than breyite. To extract the relative proportions of breyite and perovskite in each inclusion, two segments were created based on the greyscale histogram. The darker portions within each inclusion are interpreted as breyite, including all voxels at gray levels between the diamond-breyite and breyite-perovskite thresholds. The perovskite segment selects voxels with a brightness above the higher threshold.

Prior to volume estimation, known tomographic artifacts were removed from the data. First, spurious isolated voxels of apparent perovskite, created by noisy data within breyite regions, were manually removed using the SPIERS brush tool to avoid incorrect assignment as unlikely pixel sized perovskite grains. Second, partial volume averaging where the brightest phase (perovskite) is in contact with the darkest phase (diamond) can create regions of the intermediate phase (Sutton et al., 2014). In this situation, where perovskite exists along the edge of inclusions, these voxels contain perovskite and diamond. Their gray value is an average of both, creating breyite rims around perovskite grains. As no such ubiquitous breyite rims are observed in polished slices (Bulanova et al., 2010; Thomson et al., 2014) these were removed by manually assigning such rims to the perovskite phase using a SPIERS region of interest, or mask. Following corrections, thresholding allows volume estimates—however, the threshold values applied remain subjective. A sensitivity analysis examines how thresholding choices affect volume measurements. Four volume ratios for each inclusion were determined, whereby both threshold values were varied from their highest to lowest reasonable values and combined in each of four possible ways. Upper and lower bounds for volume ratios are provided using whichever two of the four reconstructions produce the highest and lowest volume fractions respectively.

2.2.3. Density Estimates

Conversion of volume to mass ratios, for composition determination, requires multiplication by the material density. As they remain fully entrapped, each inclusion is subject to internal pressure. As breyite and perovskite have different compressibilities, their relative densities change with internal pressure. Inclusion pressures were estimated using the breyite Raman barometer (Anzolini et al., 2018). Equations of state for breyite (Anzolini et al., 2016), perovskite (Ross & Angel, 1999) and CaSi-perovskite (Thomson et al., 2019) were used to determine the densities of these minerals within each inclusion, given the determined internal pressure. The perovskite component's Si content is calculated by assuming that density varies linearly between the Ti and Si-rich endmembers.

3. Results

Raman spectra from each inclusion are shown in Figure 2, with the exception of Ju5-52 for which no perovskite spectrum could be obtained. The spectra clearly constrain the mineralogy, and the subtle changes in peak positions are sufficient to estimate remanent pressure and perovskite composition. These parameters are shown in Table 1 along with the results of μCT reconstructions.

The bulk compositions of each inclusion were calculated as upper and lower bounds by Ti content. The lower bound is calculated using the minimum perovskite volume percentage from μCT, and uses the perovskite component $CaSiO_3$ mol% derived from the Raman spectrum and the perovskite density derived for that perovskite composition. The upper bound is calculated with the maximum perovskite component volume percentage and assumes that the perovskite component is pure $CaTiO_3$. This is elaborated on in Table S2. The final bulk CaSi-perovskite inclusion compositions are presented as Ti# (molar Ti/[Ti + Si]) and vary from between 0.03 and 0.60. The upper and lower bound values of the parameters are given in Table S2.

Figure 3 shows the volume reconstruction of the inclusion within diamond Col-N-18, together with two contrasting slices of this volume and the distribution of phase proportions produced by a series of random slices through the inclusion. The kernel probability distribution is broad and its peak is offset from the relative volume calculated from the μCT data. This emphasizes the improvement in compositional measurements using relative volumes recovered from μCT rather than a single polished surface.

Whilst there remain several sources of uncertainty in the compositional estimates via μCT, probably the largest stems from the volumetric proportions of the two phases (as discussed in Section 2.2.2). This is because whilst the uncertainties in pressure and perovskite Si concentration are both large in an absolute sense, neither significantly changes the perovskite component's density, so both only have a small impact on the final bulk Ti# of the bulk CaSi-perovskite inclusion.

Three specimens were scanned using both the 4× and 10× objective. For the inclusions in diamonds Ju5-52 and Ju5-13, which both have low Ti contents, there is little difference in volume estimates using different resolution objectives. The mean of the upper and lower composition bounds produced by 4× scans of the Ju5-52 and Ju5-13 inclusions produce, respectively, Ti#s which are 2.5% below and 6.6% above those produced by 10× scans. However, measurements of the inclusion in diamond Col-N-18 indicate greater perovskite volumes in the lower resolution scan; its 4× scan produces a Ti# which is 19.7% above that of its 10× scan. This inclusion also has a much more complicated geometry than the other inclusions with several large perovskite grains, many facets and small details which are clearly resolved properly only by the 10×.

4. Discussion

This study reports a large range in the Ti contents of former CaSi-perovskite inclusions (Figure 4a). To understand the cause, the variation in CaSi-perovskite compositions within subducting mafic crust at different depths must be considered. Subducting basalt entering the transition zone consists of garnet + stishovite, with all pyroxene having already dissolved into garnet solid solution as a majorite component (Ishii et al., 2019). As pressure increases, the Ca-rich endmember of garnet begins to exsolve Ca in the form of CaSi-perovskite (Ishii et al., 2019). At this point, most of the Ti in the system is expected to partition into CaSi-perovskite (Ishii et al., 2019). This is

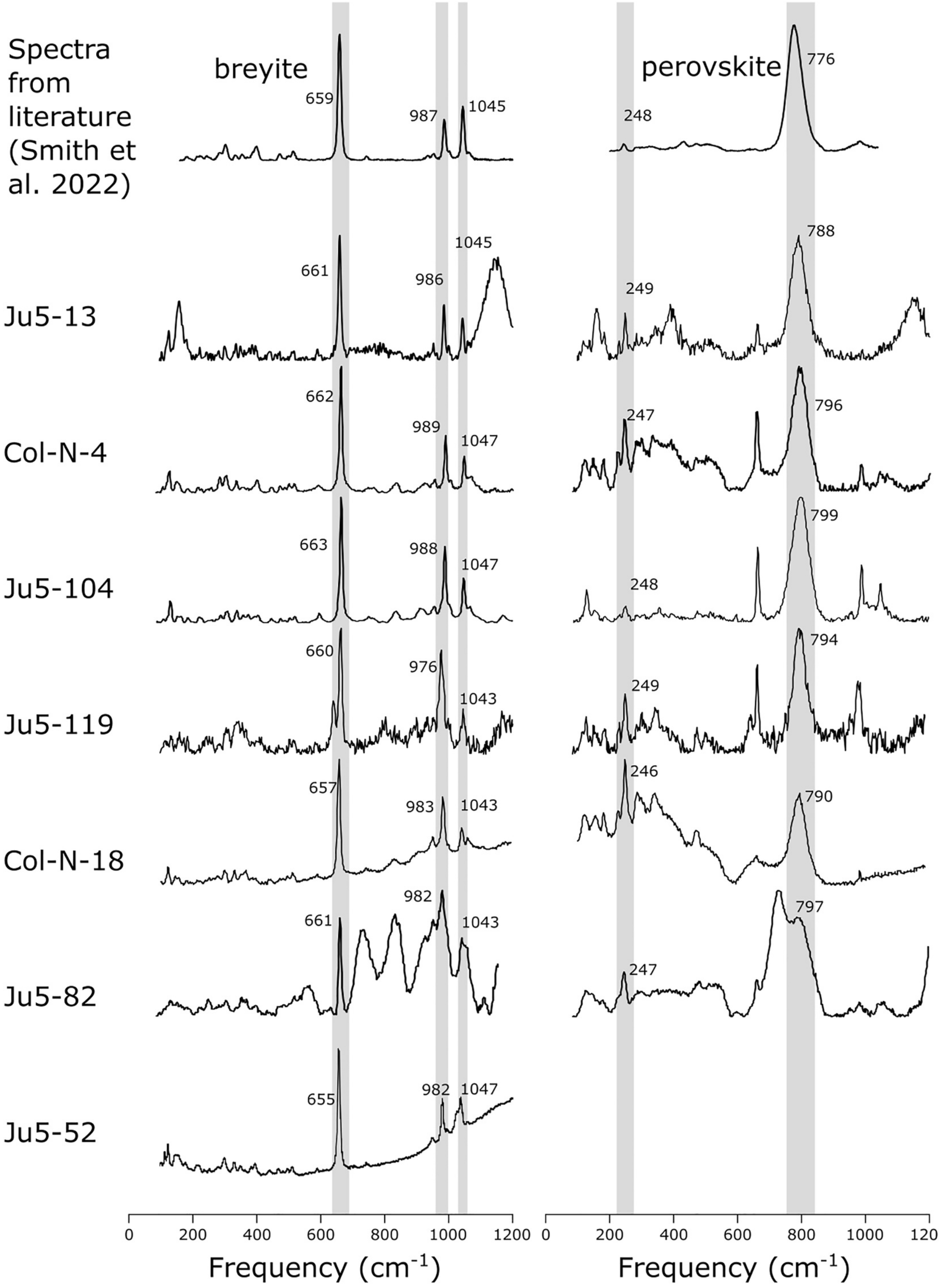

Figure 2. Breyite and perovskite Raman spectra with the diagnostic peaks highlighted with shaded bars. Spectra from the literature are provided for comparison. The noticeable shift in the 977 cm^{-1} breyite peak and the 776 cm^{-1} perovskite peak are used respectively to establish internal pressure and the Si content of the perovskite component.

demonstrated in high-pressure experiments on meta-basaltic compositions; CaSi-perovskite produced in experiments at lower pressures (<20 GPa) has the highest Ti contents (Figure 4b). As pressure increases further, the increasing modal abundance of CaSi-perovskite leads to a decrease in Ti concentration. At even higher pressures,

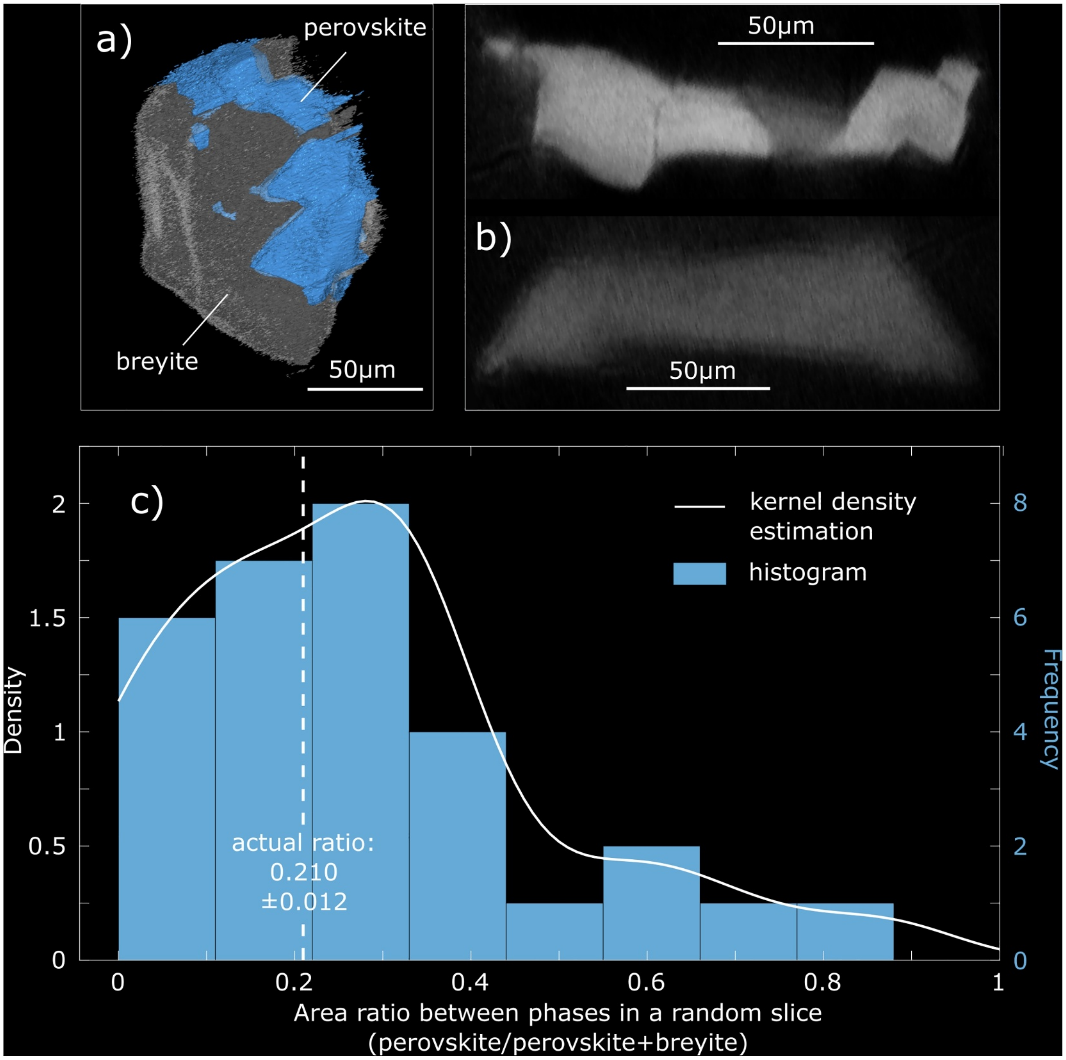

Figure 3. Errors in estimating phase proportions using a random slice through a polymineralic inclusion. (a) Volume reconstruction from µCT data. (b) Two slices through the data. The lighter material is perovskite, the intermediate is breyite and the surrounding darkness is diamond. The top slice consists largely of perovskite and the lower is pure breyite. (c) A series of random slices ($n = 30$) were taken from the µCT data of the same inclusion and the phase proportions calculated in each, then plotted here as a histogram and a kernel density estimation. Random slices can give variable, inaccurate phase proportions.

where bridgmanite becomes stable, Ti partitions into bridgmanite, resulting in much lower Ti concentrations in CaSi-perovskite (Ishii et al., 2019, 2022) (Figure 4b).

It could be argued that the high and low-Ti inclusions crystallized from environments with high or low bulk Ti concentrations respectively, or that another unseen phase may selectively partition Ti when present. However, a simpler explanation is that these inclusions sample a meta-basaltic assemblage equilibrated at different pressures, mirroring the experimental CaSi-perovskite described above. This hypothesis is supported by phase co-occurrences (observations of other non-touching inclusions which appear in the same diamonds, published in the literature). The three highest Ti# inclusions in this study (Figure 4a) all co-occur with garnet inclusions (Burnham et al., 2015; Thomson et al., 2014). The lower Ti# breyite-perovskite inclusion from Ju5-13 co-occurs with a former aluminous bridgmanite inclusion (Thomson et al., 2014). Figure 4 demonstrates that the overall range of Ti# in the inclusions matches the range in experiments, and the specific values where co-occurrences are recorded also match the range of values for the different assemblages in experiments. Thus, the most Ti-rich

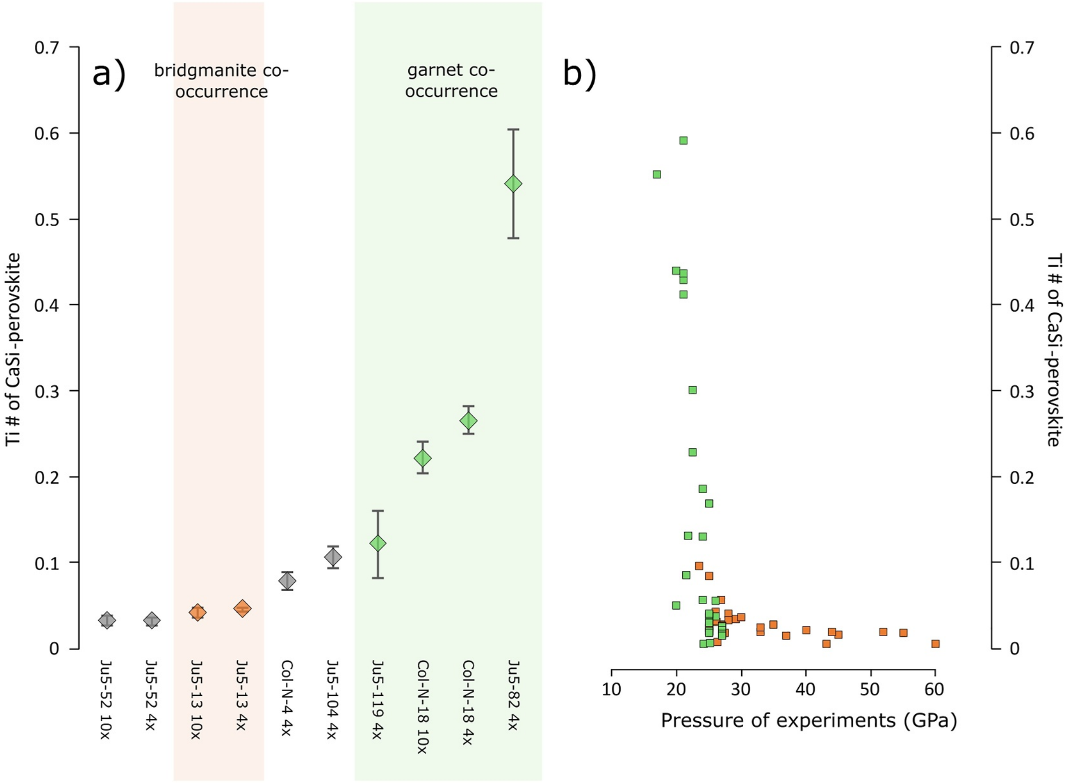

Figure 4. (a) Reconstructed bulk perovskite Ti#. Green and orange symbols represent Ca-perovskite with non-touching, coexisting garnet or former bridgmanite inclusions respectively. Markers represent the mean of maximum and minimum constraints. (b) Ti# of CaSi-perovskites produced in published experiments on mafic compositions with pressure. Green symbols: experiments produced garnet with no bridgmanite; orange symbols: experiments produce bridgmanite with or without garnet. Experimental data sources are provided in Table S3.

inclusions likely crystallized within the majoritic garnet stability field, and the more Ti-poor samples formed at greater depths, in the presence of bridgmanite. In reality the genesis of these diamonds must be more complex than simple sub-solidus trapping of metabasalt as demonstrated by trace element concentrations and the chemical compositions of other phases (Thomson, Kohn, et al., 2016; Thomson, Walter, et al., 2016; Walter et al., 2008). Nonetheless, the similarity between the Ti# of inclusions measured here and experimentally produced CaSi-perovskite is striking, so crystallization depth and the nature of coexisting phases is probably an important constraint on CaSi-perovskite inclusion chemistry.

The novel combination of techniques used here is able to reliably measure the relative abundance of breyite and perovskite phases within an inclusion, as well as estimate the composition of each phase. They produce the best measurements to date of the chemistry of unmixed CaSi-perovskite inclusions. These non-destructive techniques represent a significant advance in the study of sublithospheric diamonds and should be applied to other localities and inclusion types. Exactly the same μCT + Raman method could be used for unmixed stishovite inclusions; for other phases where the unmixed phases have more complex solid solutions (e.g., majoritic garnet, bridgmanite) μCT would have to be combined with alternative techniques to constrain inclusion chemistry. These methods can maximize the information that can be extracted from these uniquely valuable samples.

Data Availability Statement

The tomography data used for volume measurements in the study are available within the UCL data repository. Each inclusion tomogram is provided as a stack of tiff images. Data sets are available in these in-text data citation references: Rayner (2024a, 2024b, 2024c, 2024d, 2024e, 2024f, 2024g, 2024h, 2024i), etc.

Acknowledgments

We acknowledge support from Grants NE/J500033/1 and NE/J008583/1. We acknowledge beamtime session MT9809 at Diamond Light Source and thank Dr Miriam Garcia-Fernandez as the beamline scientist during this experiment. Image analysis was supported by NE/Y003586/1. We also thank Michael J. Walter, Richard Brooker and Oliver T. Lord for their discussions which contributed to this work.

References

Agrosi, G., Tempesta, G., Mele, D., Caggiani, M. C., Mangone, A., Ventura, G. D., et al. (2019). Multiphase inclusions associated with residual carbonate in a transition zone diamond from Juina (Brazil). *Lithos*, *350–351*, 105279. https://doi.org/10.1016/j.lithos.2019.105279

Anzolini, C., Angel, R. J., Merlini, M., Derzsi, M., Tokár, K., Milani, S., et al. (2016). Depth of formation of $CaSiO_3$-walstromite included in super-deep diamonds. *Lithos*, *265*, 138–147. https://doi.org/10.1016/j.lithos.2016.09.025

Anzolini, C., Prencipe, M., Alvaro, M., Romano, C., Vona, A., Lorenzon, S., et al. (2018). Depth of formation of super-deep diamonds: Raman barometry of $CaSiO_3$-walstromite inclusions. *American Mineralogist*, *103*(1), 69–74. https://doi.org/10.2138/am-2018-6184

Basham, M., Filik, J., Wharmby, M. T., Chang, P. C. Y., El Kassaby, B., Gerring, M., et al. (2015). Data Analysis WorkbeNch (DAWN). *Journal of Synchrotron Radiation*, *22*(3), 853–858. https://doi.org/10.1107/S1600577515002283

Bence, A. E., & Albee, A. L. (1968). Empirical correction factors for the electron microanalysis of silicates and oxides. *The Journal of Geology*, *76*(4), 382–403. https://doi.org/10.1086/627339

Brenker, F. E., Nestola, F., Brenker, L., Peruzzo, L., & Harris, J. W. (2021). Origin, properties, and structure of breyite: The second most abundant mineral inclusion in super-deep diamonds. *American Mineralogist*, *106*(1), 38–43. https://doi.org/10.2138/am-2020-7513

Bulanova, G. P., Walter, M. J., Smith, C. B., Kohn, S. C., Armstrong, L. S., Blundy, J., & Gobbo, L. (2010). Mineral inclusions in sublithospheric diamonds from Collier 4 kimberlite pipe, Juina, Brazil: Subducted protoliths, carbonated melts and primary kimberlite magmatism. *Contributions to Mineralogy and Petrology*, *160*, 489–510. https://doi.org/10.1007/s00410-010-0490-6

Burnham, A. D., Thomson, A. R., Bulanova, G. P., Kohn, S. C., Smith, C. B., & Walter, M. J. (2015). Stable isotope evidence for crustal recycling as recorded by superdeep diamonds. *Earth and Planetary Science Letters*, *432*, 374–380. https://doi.org/10.1016/j.epsl.2015.10.023

Genzel, P.-T., Pamato, M. G., Novella, D., Santello, L., Lorenzon, S., Shirey, S. B., et al. (2023). Geobarometric evidence for a LM/TZ origin of $CaSiO_3$ in a sublithospheric diamond. *Geochemical Perspectives Letters*, *25*, 41–45. https://doi.org/10.7185/geochemlet.2313

Guennou, M., Bouvier, P., Krikler, B., Kreisel, J., Haumont, R., & Garbarino, G. (2010). High-pressure investigations of $CaTiO_3$ up to 60 GPa using x-ray diffraction and Raman spectroscopy. *Physical Review B: Condensed Matter and Materials Physics*, *82*(13), 134101. https://doi.org/10.1103/PhysRevB.82.134101

Harte, B., & Cayzer, N. (2007). Decompression and unmixing of crystals included in diamonds from the mantle transition zone. *Physics and Chemistry of Minerals*, *34*(9), 647–656. https://doi.org/10.1007/s00269-007-0178-2

Harte, B., & Hudson, N. F. (2013). Mineral associations in diamonds from the lowermost upper mantle and uppermost lower mantle. In *Paper Presented at the Proceedings of 10th International Kimberlite Conference, New Delhi*. https://doi.org/10.1007/978-81-322-1170-9_15

Hayman, P. C., Kopylova, M. G., & Kaminsky, F. V. (2005). Lower mantle diamonds from Rio Soriso (Juina area, Mato Grosso, Brazil). *Contributions to Mineralogy and Petrology*, *149*(4), 430–445. https://doi.org/10.1007/s00410-005-0657-8

Hu, Y., Limaye, A., & Lu, J. (2020). Three-dimensional segmentation of computed tomography data using Drishti Paint: New tools and developments. *Royal Society Open Science*, *7*(12), 201033. https://doi.org/10.1098/rsos.201033

Ishii, T., Kojitani, H., & Akaogi, M. (2019). Phase relations of harzburgite and MORB up to the uppermost lower mantle conditions: Precise comparison with pyrolite by multisample cell high-pressure experiments with implication to dynamics of subducted slabs. *Journal of Geophysical Research: Solid Earth*, *124*(4), 3491–3507. https://doi.org/10.1029/2018JB016749

Ishii, T., Miyajima, N., Criniti, G., Hu, Q., Glazyrin, K., & Katsura, T. (2022). High pressure-temperature phase relations of basaltic crust up to mid-mantle conditions. *Earth and Planetary Science Letters*, *584*, 117472. https://doi.org/10.1016/j.epsl.2022.117472

Jacob, D. E., Wirth, R., Enzmann, F., Kronz, A., & Schreiber, A. (2011). Nano-inclusion suite and high resolution micro-computed-tomography of polycrystalline diamond (framesite) from Orapa, Botswana. *Earth and Planetary Science Letters*, *308*(3–4), 307–316. https://doi.org/10.1016/j.epsl.2011.05.056

Ketcham, R. A., & Koeberl, C. (2013). New textural evidence on the origin of carbonado diamond: An example of 3-D petrography using X-ray computed tomography. *Geosphere*, *9*(5), 1336–1347. https://doi.org/10.1130/GES00908.1

Kubo, A., Suzuki, T., & Akaogi, M. (1997). High pressure phase equilibria in the system $CaTiO_3$-$CaSiO_3$: Stability of perovskite solid solutions. *Physics and Chemistry of Minerals*, *24*(7), 488–494. https://doi.org/10.1007/s002690050063

Nestola, F., Merli, M., Nimis, P., Parisatto, M., Kopylova, M., De Stefano, A., et al. (2012). In situ analysis of garnet inclusion in diamond using single-crystal X-ray diffraction and X-ray micro-tomography. *European Journal of Mineralogy*, *24*(4), 599–606. https://doi.org/10.1127/0935-1221/2012/0024-2212

Rayner, B. (2024a). *Col-N-18 10x (Version 0)*. University College London. https://doi.org/10.5522/04/28043894

Rayner, B. (2024b). *Col-N-18 4x (Version 0)*. University College London. https://doi.org/10.5522/04/28043879

Rayner, B. (2024c). *Col-N-4 4x (Version 0)*. University College London. https://doi.org/10.5522/04/28043603

Rayner, B. (2024d). *Ju5-104 4x (Version 0)*. University College London. https://doi.org/10.5522/04/28044644

Rayner, B. (2024e). *Ju5-119 4x (Version 0)*. University College London. https://doi.org/10.5522/04/28044641

Rayner, B. (2024f). *Ju5-13 10x (Version 0)*. University College London. https://doi.org/10.5522/04/28044533

Rayner, B. (2024g). *Ju5-13 4x (Version 0)*. University College London. https://doi.org/10.5522/04/28044518

Rayner, B. (2024h). *Ju5-52 10x (Version 0)*. University College London. https://doi.org/10.5522/04/28044602

Rayner, B. (2024i). *Ju5-52 4x (Version 0)*. University College London. https://doi.org/10.5522/04/28044551

Ross, N. L., & Angel, R. J. (1999). Compression of $CaTiO_3$ and $CaGeO_3$ perovskites. *American Mineralogist*, *84*(3), 277–281. https://doi.org/10.2138/am-1999-0309

Stachel, T., Harris, J. W., Brey, G. P., & Joswig, W. (2000). Kankan diamonds (Guinea) II: Lower mantle inclusion parageneses. *Contributions to Mineralogy and Petrology*, *140*(1), 16–27. https://doi.org/10.1007/s004100000174

Sutton, M. D., Garwood, R. J., Siveter, D. J., & Siveter, D. J. (2012). Spiers and VAXML; A software toolkit for tomographic visualisation, and a format for virtual specimen interchange. *Palaeontologia Electronica*, *15*(2), 15.12.15T. https://doi.org/10.26879/289

Sutton, M. D., Rahman, I., & Garwood, R. (2014). *Techniques for virtual paelaeontology*. John Wiley & Sons, Ltd.

Thomson, A. R., Crichton, W. A., Brodholt, J. P., Wood, I. G., Siersch, N. C., Muir, J. M. R., et al. (2019). Seismic velocities of $CaSiO_3$ perovskite can explain LLSVPs in Earth's lower mantle. *Nature*, *572*(7771), 643–647. https://doi.org/10.1038/s41586-019-1483-x

Thomson, A. R., Crichton, W. A., Siersch, N. C., Ezad, I. S., Dobson, D. P., & Brodholt, J. P. (2025). Experimental observations of $CaSiO_3$-$CaTiO_3$ perovskites; implications for Ca-rich inclusions observed in sub-lithospheric diamonds. *Physics and Chemistry of Minerals*, *52*(2), 19. https://doi.org/10.1007/s00269-025-01321-z

Thomson, A. R., Kohn, S. C., Bulanova, G., Smith, C. B., Araujo, D., & Walter, M. J. (2016). Trace element composition of silicate inclusions in sub-lithospheric diamonds from the Juina-5 kimberlite: Evidence for diamond growth from slab melts. *Lithos*, *265*, 108–124. https://doi.org/10.1016/j.lithos.2016.08.035

Thomson, A. R., Kohn, S. C., Bulanova, G. P., Smith, C. B., Araujo, D., Walter, M. J., & Walter, M. J. (2014). Origin of sub-lithospheric diamonds from the Juina-5 kimberlite (Brazil): Constraints from carbon isotopes and inclusion compositions. *Contributions to Mineralogy and Petrology*, *168*(6), 1081. https://doi.org/10.1007/s00410-014-1081-8

Thomson, A. R., Kohn, S. C., Prabhu, A., & Walter, M. J. (2021). Evaluating the formation pressure of diamond-hosted majoritic garnets: A machine learning majorite barometer. *Journal of Geophysical Research: Solid Earth*, *126*(3), e2020JB020604. https://doi.org/10.1029/2020JB020604

Thomson, A. R., Walter, M. J., Kohn, S. C., & Brooker, R. A. (2016). Slab melting as a barrier to deep carbon subduction. *Nature*, *529*(7584), 76–79. https://doi.org/10.1038/nature16174

Timmerman, S., Stachel, T., Koornneef, J. M., Smit, K. V., Harlou, R., Nowell, G. M., et al. (2023). Sublithospheric diamond ages and the supercontinent cycle. *Nature*, *623*(7988), 752–756. https://doi.org/10.1038/s41586-023-06662-9

Walter, M. J., Bulanova, G. P., Armstrong, L. S., Keshav, S., Blundy, J. D., Gudfinnsson, G., et al. (2008). Primary carbonatite melt from deeply subducted oceanic crust. *Nature*, *454*(7204), 622–625. https://doi.org/10.1038/nature07132

Walter, M. J., Kohn, S. C., Araujo, D., Bulanova, G. P., Smith, C. B., Gaillou, E., et al. (2011). Deep mantle cycling of oceanic crust: Evidence from diamonds and their mineral inclusions. *Science*, *334*(6052), 54–57. https://doi.org/10.1126/science.1209300

Walter, M. J., Thomson, A. R., & Smith, E. M. (2022). Geochemistry of silicate and oxide inclusions in sublithospheric diamonds. *Reviews in Mineralogy and Geochemistry*, *88*(1), 393–450. https://doi.org/10.2138/rmg.2022.88.07

Woodland, A. B., Girnis, A. V., Bulatov, V. K., Brey, G. P., & Höfer, H. E. (2020). Breyite inclusions in diamond: Experimental evidence for possible dual origin. *European Journal of Mineralogy*, *32*(1), 171–185. https://doi.org/10.5194/ejm-32-171-2020

References From the Supporting Information

Hirose, K., & Fei, Y. (2002). Subsolidus and melting phase relations of basaltic composition in the uppermost lower mantle. *Geochimica et Cosmochimica Acta*, *66*(12), 2099–2108. https://doi.org/10.1016/S0016-7037(02)00847-5

Hirose, K., Fei, Y., Ma, Y., & Mao, H. (1999). The fate of subducted basaltic crust in the Earth's lower mantle. *Nature*, *397*(6714), 53–56. https://doi.org/10.1038/16225

Hirose, K., Takafuji, N., Sata, N., & Ohishi, Y. (2005). Phase transition and density of subducted MORB crust in the lower mantle. *Earth and Planetary Science Letters*, *237*(1–2), 239–251. https://doi.org/10.1016/j.epsl.2005.06.035

Irifune, T., & Ringwood, A. E. (1993). Phase transformations in subducted oceanic crust and buoyancy relationships at depths of 600–800 km in the mantle. *Earth and Planetary Science Letters*, *117*(1–2), 101–110. https://doi.org/10.1016/0012-821X(93)90120-X

Kiseeva, E. S., Litasov, K. D., Yaxley, G. M., Ohtani, E., & Kamenetsky, V. S. (2013). Melting and phase relations of carbonated eclogite at 9-21GPa and the petrogenesis of alkali-rich melts in the deep mantle. *Journal of Petrology*, *54*(8), 1555–1583. https://doi.org/10.1093/petrology/egt023

Kuwahara, H., Nomura, R., Nakada, R., & Irifune, T. (2018). Simultaneous determination of melting phase relations of mantle peridotite and mid-ocean ridge basalt at the uppermost lower mantle conditions. *Physics of the Earth and Planetary Interiors*, *284*, 36–50. https://doi.org/10.1016/j.pepi.2018.08.012

Litasov, K. D., & Ohtani, E. (2005). Phase relations in hydrous MORB at 18–28 GPa: Implications for heterogeneity of the lower mantle. *Physics of the Earth and Planetary Interiors*, *150*(4), 239–263. https://doi.org/10.1016/j.pepi.2004.10.010

Litasov, K., Ohtani, E., Suzuki, A., Kawazoe, T., & Funakoshi, K. (2004). Absence of density crossover between basalt and peridotite in the cold slabs passing through 660 km discontinuity. *Geophysical Research Letters*, *31*(24), L24607. https://doi.org/10.1029/2004GL021306